Journal Name

ARTICLE

Effects of immobilized VEGF on endothelial progenitor cells cultured on silicon substituted and nanocrystalline hydroxyapatites

Received 00th January 20xx,
Accepted 00th January 20xx

DOI: 10.1039/x0xx00000x

www.rsc.org/

M. J. Feito,[a,b] M. C. Serrano,[c] M. Oñaderra,[a] M. C. Matesanz,[a] S. Sánchez-Salcedo,[d,e], D. Arcos,[d,e] M. Vallet-Regí,[d,e] and M. T. Portolés[a,b,*]

Vascular endothelial growth factor (VEGF) plays an essential role in angiogenesis and vascular homeostasis. Endothelial progenitor cells (EPCs) are primitive bone marrow cells participating in neovascularization and revascularization processes, which also promote bone regeneration. Synthetic hydroxyapatite (HA) has been widely used in bone repair and implant coating. In HA-based materials, small levels of ionic substitution by silicon (Si) have significant effects on osteoclastic and osteoblastic responses. Moreover, nanocrystalline hydroxyapatites (nano-HA) display enhanced bioreactivity and beneficial effects in bone formation. In this work, the angiogenic potential of VEGF-121 adsorbed on crystalline and nanocrystalline HAs with different Si proportion is evaluated with endothelial-like cells derived from EPCs cultured on nano-HA, nano-SiHA0.25, nano-SiHA0.4, HA, SiHA0.25 and SiHA0.4 disks. The Si amount incorporated for x = 0.25 is enough to yield changes in the textural parameters and surface charge without decomposing the HA phase. Si substitution for x = 0.4 does not result in pure Si-substituted apatites. Si probably remains at the grain boundaries as amorphous silica in nano-SiHA0.4 and SiHA0.4 is decomposed in α-TCP and HA after 1150 ºC treatment. Immobilized VEGF on nano-HA, nano-SiHA0.25, nano-SiHA0.4, HA, SiHA0.25 and SiHA0.4 maintains its function exerting a local regulation of the cell response. The crystallite size and topography of nanocrystalline HAs could produce insufficient and weak contacts with endothelial-like cells triggering anoikis. Concerning Si proportion, the best results are obtained with SiHA0.25/VEGF and nano-SiHA0.25/VEGF disks. All these results suggest the potential utility of SiHA 0.25/VEGF and nano-SiHA 0.25/VEGF for bone repair and tissue engineering by promoting angiogenesis.

Introduction

Tissue engineering strategies are often based on the combination of cells, biomaterials and growth factors in order to promote the regeneration of damaged tissues.[1] The success of these combinations depends on their capability to stimulate both tissue regeneration and neovessel formation (angiogenesis) after implantation.[2,3] Different growth factors have been incorporated into engineered systems to regulate cell signaling, migration, proliferation and differentiation as well as to promote adequate vascularization.[2] Numerous studies evidence that surface immobilized growth factors present enhanced stability and prolonged function, indicating that cell responses can be regulated by material properties and by growth factors at the implant site.[4-7] Several growth factors are known to be involved in angiogenesis and vascular homeostasis.[8] Among them, vascular endothelial growth factor (VEGF) is one of the most prominent due to its essential role for regulating angiogenesis, endothelial cell function and signaling.[9] Several members of the VEGF family have been described: VEGF A, B, C, D, E and placenta growth factor (PDGF). VEGF-A exerts an important activity on vascular endothelial cells, promoting angiogenesis and increasing microvascular permeability.[10] Alternative splicing of the VEGF-A gene yields four isoforms of 121, 165, 189, and 206 amino acids, and other less frequent splice variants. VEGF-121 lacks of 15 basic amino acids within the 44 residues encoded by exon 7 and for this reason this molecule is a weakly acidic protein, does not bind heparin, and is secreted, playing a role of prime importance in angiogenesis.[10] VEGF-165, in part secreted and in part matrix bound, is involved in the activation of proteinase cascades, leading to release of matrix-bound VEGF isoforms which provide an amplification mechanism.[11] Both VEGF-189 and VEGF-206 are basic, with a high affinity for heparin, and remain sequestered in the extracellular matrix,

[a] Department of Biochemistry and Molecular Biology I/Faculty of Chemistry, Universidad Complutense de Madrid, Spain.
[b] Instituto de Investigación Sanitaria San Carlos IdISSC, Spain.
[c] Hospital Nacional de Parapléjicos Servicio de Salud de Castilla-La Mancha, Toledo, Spain.
[d] Department of Inorganic and Bioinorganic Chemistry/Faculty of Pharmacy, Universidad Complutense de Madrid, Instituto de Investigación Hospital 12 de Octubre i+12, Spain.
[e] Networking Research Center on Bioengineering/Biomaterials and Nanomedicine, CIBER-BBN, Spain.

* Corresponding author. E-mail address: portoles@quim.ucm.es.

presumably bound to heparan sulfate proteoglycans.[11] The different VEGF forms bind to receptors that exhibit tyrosine-kinase activity. VEGF-A binds to receptors VEGFR-1 and VEGFR-2 with high affinity, playing major roles in physiological as well as pathological angiogenesis, including tumor angiogenesis.[12] In addition, VEGF-A has other important functions, including immunosuppression and autocrine effects on tumor cell function.[13] The immobilization of growth factors to biomaterial surfaces has emerged as a method for tissue engineering applications, improving the growth factor stability, the persistence of its delivery to cells and limitating its diffusion to the other tissues.[4,14,15]

Concerning bone tissue, the angiogenic process is a key regulatory mechanism that accompanies bone regeneration acting as limiting factor for the healing process.[16] VEGF is involved in both the angiogenesis and the maturation of osteoblasts, ossification, and bone turnover. Thus, osteogenesis and vascularization are coupled during bone development and growth.[17-19]

Endothelial progenitor cells (EPCs) are primitive bone marrow cells participating in postnatal neovascularization / revascularization processes, which also promote bone regeneration.[16] These cells can be isolated from peripheral blood, expanded and used for tissue engineering to promote revascularization of injured tissues.[16,20-22] An increasing number of studies are documenting their potential use not only as repair tools but also as biomarkers in numerous diseases including cardiovascular pathologies, kidney disease, stroke and, more recently, neurodegenerative disorders.[23,24] These cells are also the focus of diverse translational and clinical trials for bone regeneration.[25] Concerning biomaterials for bone tissue, synthetic hydroxyapatite (HA) has been widely used in bone repair[26] and for application as implant coating to improve the performance of bone implants.[27] Small levels of ionic substitution by silicon (Si) have significant effects on osteoclastic and osteoblastic responses both *in vitro* and *in vivo*.[28] The favourable effects of Si substitution in HA on bone cells have been related to passive and active mechanisms as material solubility increase, topographical changes, grain size reduction, surface charge modifications and ionic release of Si and Ca.[29-33] On the other hand, nanocrystalline hydroxyapatites (nano-HA) display enhanced bioreactivity *in vivo* with respect to HA, showing beneficial effects in the early stages of bone formation.[34,35]

In order to know the angiogenic potential of VEGF-121 (2,5 µg) adsorbed on disks of crystalline and nanocrystalline hydroxyapatites with different Si proportion (nominal formula $Ca_{10}(PO_4)_{6-x}(SiO_4)_x(OH)_{2-x}$ with x = 0, 0.25 and 0.40), EPCs were cultured on nano-HA, nano-SiHA 0.25, nano-SiHA 0.4, HA, SiHA 0.25, and SiHA 0.4 disks with or without immobilized VEGF-121. EPC morphology, adhesion and proliferation on the surface of all these hydroxyapatite disks were evaluated by confocal microscopy, scanning electron microscopy and cell counting. In this *in vitro* comparative study, three different aspects were taken into account regarding effects on EPCs: the immobilized VEGF-121 action, the influence of different Si contents and the nanocrystallinity degree. As far as we are aware, this is the first time that the effects of the silicon levels and the microstructural properties of SiHA are studied on endothelial cells, which is especially relevant for the VEGF immobilization on the surface and their potential angiogenic capabilities.

Experimental

Synthesis of materials. Samples of pure and silicon-substituted HA were prepared by aqueous precipitation reaction of $Ca(NO_3)_2 \bullet 4H_2O$, $(NH_4)_2HPO_4$ and $Si(CH_3CH_2O)_4$ (TEOS) solutions. The amounts of reactants were calculated on the assumption that silicon would substitute phosphorus. Three different compositions were prepared with nominal formula $Ca_{10}(PO_4)_{6-x}(SiO_4)_x(OH)_{2-x\square x}$, with x = 0, 0.25 and 0.40 for samples HA, SiHA-0.25 and SiHA-0.4, respectively, and □ means vacancies at the hydroxyl position. A 1 M solution of $Ca(NO_3)_2 \bullet 4H_2O$ was added to $(NH_4)_2HPO_4$ and TEOS solutions of stoichiometric concentration to obtain the compositions described above. The mixtures were stirred for 12 h at 80 °C. The pH was kept at 9.5 by NH_3 solution addition. During the reaction, the pH was continuously adjusted to 9.5 to ensure constant conditions during the synthesis. The precipitated powders were washed with deionized water until total remove of nitrates. Thereafter, the powders were dried at 100 ºC overnight, milled and sieved to collect the grain fraction below 50 µm. Fractions of 300 mg of the powders were then shaped into disks of 12 mm in diameter. Half of the disks was treated at 700 ºC for 3 hours under air atmosphere. These 700 ºC treated materials will be thereafter referred as nano-HA, nano-SiHA0.25 and nano-SiHA0.4. The rest of the disks were treated at 1150 ºC for 3 hours under air atmosphere and will be referred as HA, SiHA0.25 and SiHA0.4.

Characterization of materials. X-ray diffraction experiments were performed using a Philips X'Pert diffractometer equipped with Cu Kα radiation (wavelength 1.5406 A). The disks were powdered in a vibratory mill and XRD patterns were collected in the range of 10 to 80 2θº with a step size of 0.02º and a counting time of 4 s per step. In order to determine the microstructure of the synthesized samples, Rietveld refinements of the structures were carried out for the samples treated at 700 ºC, as well as for the samples treated at 1150 °C. The scale factor, atomic positions, isotropic temperature factors, and patterns parameters (peak widths, cell dimensions, zero shift of 2θ °, background points interpolation, etc.) were also varied. The refinements were performed using the atomic position set and the space group of the HA structure *P*63/*m*, No. 176 by means of the FullProf 2000 computer program.[36,37] The instrumental resolution function (IRF) of the diffractometer was obtained from a very-well-crystallized LaB_6 sample and taken into account in a separate input file. The pseudo-Voigt profile function

of Thompson, Cox, and Hastings was used with an asymmetry correction at low angle.[38]

Disk-shaped pieces were investigated by scanning electron microscopy (SEM) using a field emission JEOL JSM-6335F microscope (Tokyo, Japan) at an acceleration voltage of 10 kV.

The textural properties of the materials were determined by nitrogen absorption porosimetry by using a Micromeritics ASAP 2020. To perform the N_2 measurements, the samples were previously degassed under vacuum for 24 h at room temperature. The surface area was determined using the Brunauer–Emmett–Teller (BET) method.[39] The pore size distribution between 0.5 and 40 nm was determined from the adsorption branch of the isotherm by means of the Barrett–Joyner–Halenda (BJH) method.[40] FTIR spectra were obtained with a Thermo Nicolet nexus spectrometer, using the KBr pellet method. Zeta potential determination by electrophoretic mobility was carried out in a Zetasizer Nano ZS (Malvern Instruments) by suspending MBG particles in phosphate buffered solution at pH 7.4 (PBS).

VEGF adsorption on hydroxyapatite disks. Nano-HA, nano-SiHA0.25, nano-SiHA0.4, HA, SiHA0.25 and SiHA0.4 disks were introduced into 24 well culture plates (CULTEK S.L.U., Madrid, Spain) and sterilized under UV light during 1 hour for each side in a sterile environment. Adsorption of VEGF on the disk surface was carried out through non-covalent binding by incubation of each disk with 5 μg/ml of VEGF (VEGF-121, 583204, Biolegend, San Diego, CA, USA) in phosphate buffered saline (PBS) in a final volume of 500 μl and moderate shaking at 4 °C for different times. Controls of each disk type without VEGF were carried out in parallel. After 0, 0.5 and 24 hours of incubation, the concentration of VEGF in the supernatant was analyzed by using an Enzyme Linked Immuno-Sorbent Assay (ELISA, Cloud-Clone Corp, USA) and the adsorbed VEGF amount on each disk surface was indirectly calculated as the difference between the VEGF levels at the initial time and after each incubation time. To evaluate the spontaneous desorption of adsorbed VEGF on each disk type, the supernatant was aspirated after 24 hours of incubation with VEGF, disks were then incubated with 500 μl of PBS at 4 ºC for 36 and 72 hours (60 and 96 hours after the initial time), and the concentration of desorbed VEGF in the supernatant was analyzed by ELISA. In this assay, a capture human antibody highly specific for VEGF was used to coat the wells of the microtiter strip plate. Samples, standard, and blank (100 μl each) were incubated with the capture antibodies and the subsequent binding of biotin-conjugated antibody specific to VEGF-A to the analyte was completed during 1 hour at 37 ºC. Any excess of unbound analyte and secondary antibody was removed by using 350 μl of wash solution (3×). The avidin conjugated to horseradish peroxidase (100 μl) was then added to every well, during 30 min at 37 ºC, and afterwards incubation excess conjugate was removed by careful washing. A chromogen substrate (3,3',5,5'-tetramethylbenzidine, TMB, 90 μl) was added to the wells resulting in the progressive development of a blue complex with the conjugate. The enzyme-substrate reaction was finished by the addition of 100 μl of sulphuric acid solution and the color change was measured spectrophotometrically at a wavelength of 450 nm ± 10 nm. The color intensity of the produced complex is directly proportional to the concentration of VEGF-A present in the samples and standards. The standard curve was carried out according to the manufacturer's instructions. The sensitivity of these assays was less than 6.1 pg/ml and their inter assay variation coefficients were <12 %.

Adsorption of bovine serum albumin (BSA) on HA disks. For BSA adsorption experiments, nano-HA, nano-SiHA0.25, nano-SiHA0.4, HA, SiHA0.25 and SiHA0.4 disks with or without immobilized VEGF were incubated with a solution of BSA (A2058, Sigma-Aldrich, St. Louis, MO, USA) at 4 mg/ml in PBS and moderately shaken for 4 h at 37 ºC. No significant difference was detected between the amount of adsorbed protein after 4 h and 24 h. After incubation, the supernatant obtained was analyzed by UV-Vis spectroscopy and the adsorbed protein amount was indirectly calculated as the difference in protein concentration before and after BSA adsorption using a value of 0.667 as extinction coefficient E (279 nm, 1cm and 0.1 % solution of BSA).

Isolation and culture of EPC-derived cells on HA disks with or without immobilized VEGF. For the isolation of EPCs, porcine peripheral blood was obtained from healthy Large White pigs (35–45 kg), supplied by the Universitary Hospital ''12 de Octubre'' (Madrid, Spain). Porcine endothelial-like cells at an early differentiation stage (EC1) derived from EPCs were used in this study as angiogenic cells expressing von Willebrand factor and endothelial NO synthase.[41] To obtain EC1, whole pig blood was diluted (1:1, v/v) in PBS (pH 7.2) with 0.1 % BSA and 0.6 % sodium citrate. Mononuclear cells (MNCs) were isolated using a density gradient formed with Histopaque-1077 solution (Sigma-Aldrich, St. Louis, MO, USA) in AccuspinTM tubes (Sigma-Aldrich, St. Louis, MO, USA). After centrifugation at 800*g* for 30 min at room temperature, the MNC layer was carefully collected and seeded in EGM-2 medium (Endothelial Growth Medium containing hydrocortisone, FGF-2, VEGF, R3-insulin-like growth factor-1, ascorbic acid, epidermal growth factor, heparin, gentamicin sulfate and amphotericin-B, Lonza, Walkersville, MD, USA) onto 75 cm^2 polystyrene culture flasks (Corning, NY, USA) at a density of 2-3 x 10^5 cells/cm^2 under 5 % CO_2 atmosphere at 37 ºC. The culture medium was replaced at 96 h and then every 48 h for three weeks. These EC1 cells were washed with PBS, harvested using 0.25 % trypsin–EDTA solution and cultured on nano-HA, nano-SiHA0.25, nano-SiHA0.4, HA, SiHA0.25 and SiHA0.4 disks with or without immobilized VEGF at a density of 2 x 10^4 cells/ml into 24 well culture plates (CULTEK S.L.U., Madrid, Spain) in EGM-2 medium under a CO_2 (5 %) atmosphere at 37 ºC for 5 days. To evaluate cell proliferation, the attached cells were washed with PBS and harvested using 0.25 % trypsin-EDTA solution for 15 min. The reaction was stopped with complete culture medium and cells were counted with a Neubauer hemocytometer.

Morphological studies by confocal laser scanning microscopy. After fixation with 3.7 % paraformaldehyde in PBS for 10 min, samples cultured with EC1 were washed with PBS and permeabilized with 0.1 % Triton X-100 for 3 to 5 min. The

samples were then washed with PBS and pre-incubated with PBS containing 1 % BSA for 20 to 30 min. Then, cells were incubated with rhodamine phalloidin (1:40 v/v Molecular Probes) for 20 min to stain F-actin filaments. Samples were then washed with PBS and cell nuclei were stained with DAPI (4'-6-diamidino-2'-phenylindole; Molecular Probes), at 3 µM in PBS. After staining and washing with PBS, cells were examined using a Leica SP2 Confocal Laser Scanning Microscope. Rhodamine fluorescence was excited at 540 nm and measured at 565 nm. DAPI fluorescence was excited at 405 nm and measured at 420–480 nm.

Morphological studies by scanning electron microscopy. EC1 cells cultured on nano-HA, nano-SiHA0.25, nano-SiHA0.4, HA, SiHA0.25 and SiHA0.4 disks were fixed with glutaraldehyde (2.5 % in PBS) for 45 min. Sample dehydration was performed by slow water replacement using series of ethanol solutions (30, 50, 70, 90 %) for 15 min each with a final dehydration in absolute ethanol for 30 min, followed by a drying step at room temperature and under vacuum. Afterwards, the pieces were mounted on stubs and coated in vacuum with gold-palladium. Samples were then examined with a JEOL JSM-6400 scanning electron microscope.

Statistics. Data are expressed as means + standard deviations of a representative of three repetitive experiments carried out in triplicate. Statistical analysis was performed by using the Statistical Package for the Social Sciences (SPSS) version 11.5 software. Statistical comparisons were made by analysis of variance (ANOVA). Scheffé test was used for post hoc evaluations of differences among groups. In all statistical evaluations, $p < 0.05$ was considered as statistically significant.

Results and discussion

The success of engineered systems for tissue repair depends on their capability to stimulate both tissue regeneration and angiogenesis after implantation.[2,3] VEGF has been immobilized in different scaffolds designed for tissue engineering in order to promote angiogenesis.[4] Concerning materials for bone repair, HA is widely used because its composition is closest to that of bone mineral.[42] Small levels of ionic substitution by Si in HA have been shown to have significant effects on solubility, bioactivity, osteoclastic and osteoblastic response both *in vitro* and *in vivo*.[28,35,43] On the other hand, nano-HAs with higher surface area, smaller crystal size and enhanced bioreactivity, can be prepared avoiding the high temperature sintering process of these bioceramics.[42,44-46] In the present study, the angiogenic potential of VEGF-121 immobilized on Si-substituted and nano-HAs was evaluated with EPC-derived EC1 cells cultured on nano-HA, nano-SiHA0.25, nano-SiHA0.4, HA, SiHA0.25 and SiHA0.4 disks, with or without immobilized VEGF. This *in vitro* comparative study allowed knowing three different aspects on the behavior of EPC-derived cells: immobilized VEGF action, influence of different Si contents and nanocrystallinity. Prior to VEGF immobilization, all these HAs were characterized by XRD, N_2 absorption porosimetry, FT-IR spectroscopy and ζ potential measurements.

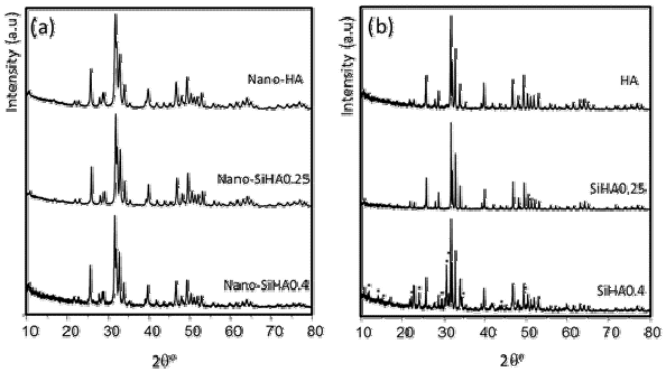

Figure 1. XRD patterns of **(a)** samples prepared at 700 ºC and **(b)** samples prepared at 1150 ºC. All the diffraction maxima correspond to a hydroxyapatite phase except those signed by (*), which correspond to α-TCP.

Figure 1.a shows the XRD patterns of samples treated at 700º C. In the three cases, all the diffraction maxima are assigned to a HA phase. The coherent diffraction domains, commonly named crystallite size, were calculated from the Rietveld refinements. **Table 1** shows that the crystallite sizes are below 100 nm in the three samples, pointing out the nanocrystalline microstructure of these materials. The values in brackets shown in Table 1 are a measure of the degree of anisotropy and indicate that HAs and Si-substituted HAs exhibit crystallites with around a 10 % of anisotropy when are prepared at 700º C. This crystal growth anisotropy would result in needle shaped crystallites with the axial direction along the c axis of the HA unit cell, as it has been observed for very similar compounds.[47]

Table 1. Crystallite size and textural parameters of the synthesized samples.

Sample	Crystallite size[1] (nm)	S_{BET} ($m^2 \cdot g^{-1}$)	Pore Volume ($cm^3 \cdot g^{-1}$)	Pore Size (nm)
nano-HA	30.9 (3.1)	17.00	0.040	8.7
HA	197.8 (4.6)	2.05	0.003	5.2
nano-SiHA0.25	71.4 (7.5)	25.90	0.170	26.8
SiHA0.25	338.8 (46.6)	1.23	0.003	6.4
nano-SiHA0.4	32.8 (4.0)	14.60	0.060	15.8
SiHA0.4	283.7 (43.1)	1.40	0.003	8.3

[1]: The standard deviations appearing in the crystallite size are a measure of the degree of anisotropy, not of the estimated error. S_{BET}: Specific surface area calculated by the Brunauer-Emmett-Teller (BET) method.

Figure 1.b shows the XRD patterns of samples treated at 1150 ºC. Samples HA and SiHA0.25 show well resolved diffraction maxima, which are assigned to a unique apatite-like phase. In the case of SiHA0.4, the XRD pattern show well resolved maxima corresponding to two different phases: a major HA phase and a minor alpha polymorph of tricalcium phosphate (α-TCP) phase. The phase percentages obtained from Rietveld refinements were 61 % and 39 % for HA and α-TCP, respectively. The decomposition of SiHA0.4 into HA and TCP can be explained in terms of the limited amount of Si that can be incorporated into the HA structure. The substitution of PO_4^{3-} by SiO_4^{4-} entails the formation of vacancies at the anionic positions as well as tetrahedral distortion at the P sites. When the amount of Si incorporated is too high, the subsequent thermal treatment leads to the decomposition of the apatite phase into HA and TCP. α-TCP is the high temperature phase of $Ca_3(PO_4)_2$. This phase is commonly obtained with reaction temperatures between 1250 and 1500 ºC.[48] In our case, for a thermal treatment at 1150 ºC the expected segregated phase would be β-TCP, however, α-TCP is formed as a consequence of the presence of Si, which stabilizes the formation of the alpha polymorph at temperatures below 1350 ºC.[49]

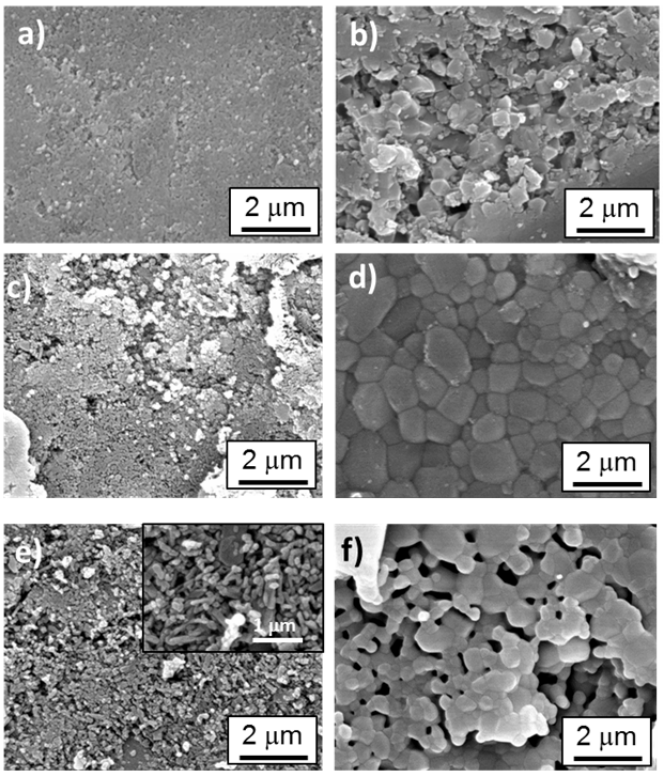

Figure 2. Scanning electron macrographs (magnification x 10000) obtained from **(a)** nano-HA, **(b)** HA, **(c)** nano-SiHA0.25, **(d)** SiHA0.25, **(e)** nano-SiHA0.4, **(f)** SiHA0.4. The inset in figure 2.e shows a higher magnification (x 20000) of nano-SiHA0.4

The size and morphological features of the samples were confirmed by SEM (**Figure 2**). SEM micrographs obtained for disks treated at 700º C show porous surfaces constituted by nanoparticles. Higher magnifications (see the inset in **Figure 2e**) evidence the nanometrical size of the crystallites as well as a rod-shaped morphology, indicating an anisotropic crystal growth of these samples.

Samples treated at 1150ºC show very different microstructural characteristics. In agreement with the crystallite size calculated by XRD, SEM images of crystalline samples show larger particles ranging in size between 0.2 and 1 micrometre, as a consequence of the sintering process undergone during the thermal treatment. HA and SiHA 0.4 samples show some degree of porosity as a consequence of the formation of microstructural defects during the sintering process. In the case of SiHA0.4 the grain boundaries seems to be fused by a melted phase that could by associated with an excess of silica accumulated at the grain boundaries. On the contrary, SiHA0.25 (**Figure 2d**) shows a well sintered surface, with grains exhibiting polyhedral shapes and lower degree of microstructural defects.

Table 1 also shows the surface area and porosity parameters for the synthesized samples. The apatites treated at low temperature show surfaces areas about 15 – 25 $m^2 \bullet g^{-1}$ and porosities in the range of 0.04 and 0.17 $cm^3 \bullet g^{-1}$. It must be highlighted that sample nano-SiHA0.25 showed surface area and porosity values significantly higher than the rest of the samples. As expected, the samples treated at 1150 ºC undergo a reduction of surface and porosity as a consequence of the sintering process during the thermal treatment.

Figure 3 shows the FT-IR spectra of both nano and highly crystalline samples. The absorption bands at 567 and 601 cm^{-1} correspond to the bending mode of O-P-O bonds, whereas the absorption bands at 962, 1033 and 1091 cm^{-1} correspond to the stretching vibration modes of the P-O bond of the phosphate groups. The bands at 632 and 3571 cm^{-1} correspond to the librational mode and stretching mode of the hydroxyl groups, respectively.

It must be highlighted that the librational mode of the hydroxyl groups is very weak in SiHA0.25 and SiHA0.4 samples. This fact can be explained in terms of the vacancies created at the OH positions when SiO_4^{4-} substitutes PO_4^{3-} especially after the thermal treatment at high temperature, following the mechanism proposed by Gibson et al.[50]

$$10Ca^{2+} + (6\text{-}x)\ PO_4^{3-} + x\ SiO_4^{4-} + 2\text{-}x\ OH^- \longrightarrow Ca_{10}(PO_4)_{3-x}(SiO_4)_x(OH)_{2-x\square x}$$

where □ means vacancies. The higher the Si content, the higher the number of vacancies, so that the librational mode band becomes weaker as a function of the substitution degree.

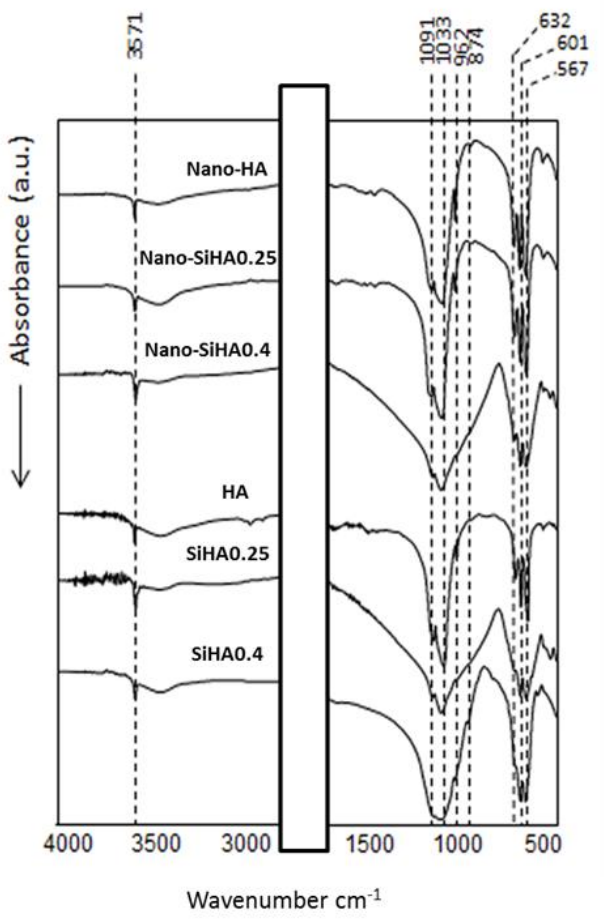

Figure 3. FTIR spectra collected from the synthesized samples.

The zeta potential values for samples heat-treated at 700 ºC show that the surface charge changes toward more negative values as a function of the Si substitution degree (**Figure 4**). These data are in full agreement with the extra negative charge introduced by silicate anions, SiO_4^{4-}, when substitute phosphates, PO_4^{3-}. The thermal treatment at 700 ºC seems to be too low to fully incorporate silicate anions within the bulk of the apatite crystals, and most of silicate remain entrapped at the grain surface.[47] Our results point out this fact, as the variation of the surface charge is almost linear respect to the Si incorporated. After the thermal treatment at 1150 ºC, the surface charge of the three compositions shifts towards more negative values (Figure 3). This fact could be explained by the loss of divalent anions such as HPO_4^{3-} or residual carbonates that could remain at 700 ºC, but not after being treated at 1150 ºC. Curiously, the differences of zeta potential values of the three compositions become non-significant after the treatment at high temperatures, pointing out that silicate anions in samples SiHA0.25 and SiHA0.4 have been incorporated within the bulk of the apatite grains and are not concentrated at the grain surface as occurred in nano-SiHA0.25 and nano-SiHA0.4.

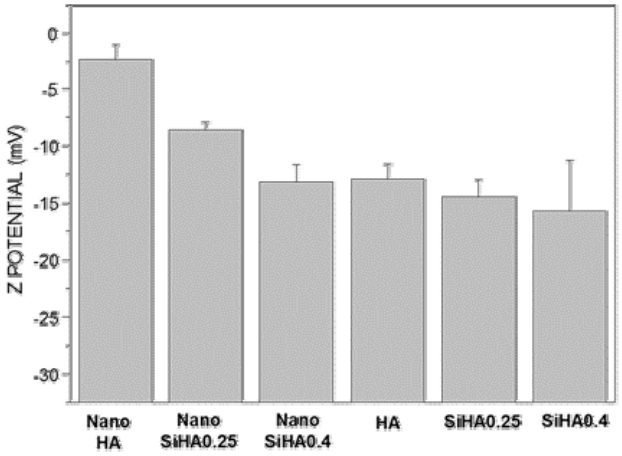

Figure 4. Zeta potential measurements obtained from the synthesized samples.

After characterization of nano-HA, nano-SiHA0.25, nano-SiHA0.4, HA, SiHA0.25 and SiHA0.4 disks, the VEGF adsorption on the surface of all these disk types was carried out through non-covalent binding by incubation of each disk type with 500 µl of a solution of this factor in PBS (5 µg/ml) and the immobilized VEGF was indirectly evaluated after different times by ELISA, measuring the non-adsorbed VEGF (ng/ml). To measure the VEGF spontaneous desorption from disks, after 24 h of incubation with this factor, VEGF/disks were incubated with 500 µl of PBS for 36 and 72 hours (60 and 96 hours after the initial time) and desorbed VEGF was also analyzed by ELISA.

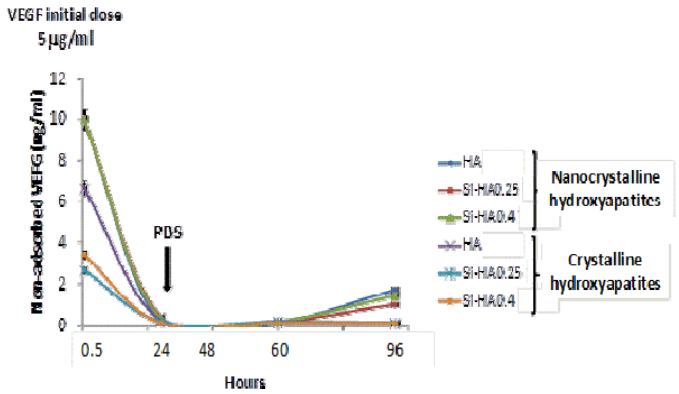

Figure 5. Indirect evaluation of VEGF adsorption and spontaneous desorption on disks of nanocrystalline and crystalline HAs with different Si proportions. Disks were incubated with 500 µl of a solution of 5 µg/ml VEGF-A for different times. Non-adsorbed VEGF (ng/ml) was determined by ELISA. After 24 h of incubation with VEGF, VEGF/disks were incubated with 500 µl of PBS for 36 and 72 hours (60 and 96 hours after the initial time) and desorbed VEGF was analyzed by ELISA.

As it can be observed in **Figure 5**, the binding of VEGF was reached efficiently in all these materials and 2.5 μg were adsorbed on each disk after 24 h in our experimental conditions. Very low levels (lower than 2 ng/ml) of desorbed VEGF were observed in all cases 96 hours after the initial time, thus indicating the effective immobilization of VEGF on the different disks evaluated. This dose was chosen in agreement with recent studies by others.[51]

It is well known that blood and interstitial fluid proteins adsorb immediately to the surface of any biomaterial after in vivo implantation, determining the implant success or failure.[52,53] On the other hand, the adhesion of serum proteins to biomaterials has also been linked to the increase of both bacteria-surface interaction and platelet adhesion with risk of bacterial colonization and thrombogenicity, respectively.[54-56] In the present study, the adsorption of BSA on the surface of nano-HA, nano-SiHA0.25, nano-SiHA0.4, HA, SiHA0.25 and SiHA0.4 disks was measured by spectroscopy after VEGF adsorption. As it can be observed in **Figure 6**, the amount of BSA adsorbed after 4 h on the surface of crystalline HAs was significantly lower than on the surface of nanocrystalline samples in agreement with previous studies.[57] No significant difference was detected between the amount of adsorbed protein after 4 h and 24 h.

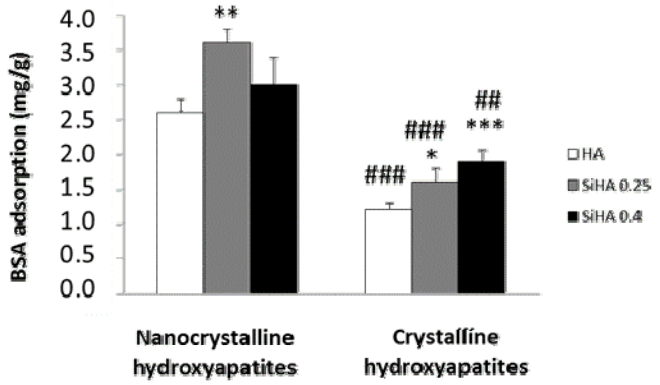

Figure 6. Evaluation of BSA adsorption after 4 h on disks of nanocrystalline and crystalline HAs with different Si proportions after VEGF adsorption. * Comparisons between each Si-substituted HA and HA, # Comparisons between each nanocrystalline and crystalline HAs. Statistical significance: ***, ### $p < 0.005$; **, ## $p < 0.01$; * $p < 0.05$.

In order to evaluate the angiogenic potential of VEGF (2,5 μg) adsorbed on nano-HA, nano-SiHA0.25, nano-SiHA0.4, HA, SiHA0.25 and SiHA0.4 disks, porcine endothelial-like cells at an early differentiation stage (EC1) derived from EPCs were cultured on all these disk types with or without immobilized VEGF.

EPCs are circulating premature cells which can differentiate into endothelial cells depending on the local environment and can be used as an alternative to primary endothelial cells for tissue engineering.[58] These angiogenic cells were characterized in previous studies by the expression of von Willebrand factor and endothelial nitric oxide synthase.[41] In the present study, cell morphology, adhesion and proliferation on the surface of these six types of HA disks with or without immobilized VEGF were evaluated by confocal microscopy, scanning electron microscopy (SEM) and cell counting. Three different aspects were compared: the immobilized VEGF action, the influence of different Si content and the nanocrystallinity.

All the disks supported EPC-derived cell adhesion and growth on their surface. As it can be observed in **Figures 7** and **8**, EC1 cells spread on all these biomaterials showing a distinctive actin network and presenting their typical morphology. However, cell number on disks without VEGF was lower than on those with VEGF, thus evidencing the stability and functionality of the surface immobilized growth factor. The effects of adsorbed VEGF (2.5 μg) on the proliferation of EPC-derived cells on disks of nanocrystalline and crystalline SiHA 0.25 are shown in **Figure 9A**. Similar effects of adsorbed VEGF on cell proliferation were observed with the other hydroxyapatites (data not shown). Recent findings provide evidence that cell number of both primary and immortalised endothelial cells were significantly enhanced on VEGF-functionalised poly(ε-caprolactone) scaffolds showing that this growth factor displays enhanced stability and function.[4]

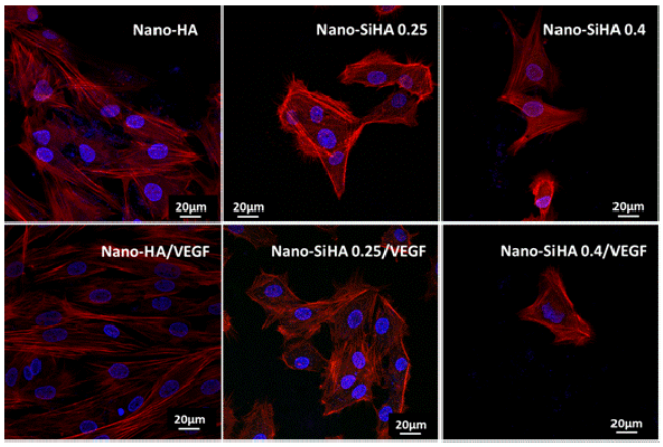

Figure 7. Morphology of EPC-derived cells on disks of nanocrystalline HAs with different Si proportions with or without adsorbed VEGF (2.5 μg) observed by confocal

microscopy after 5 days of culture. Actin was stained with rhodamine-phalloidin (red) and cell nuclei with DAPI (blue).

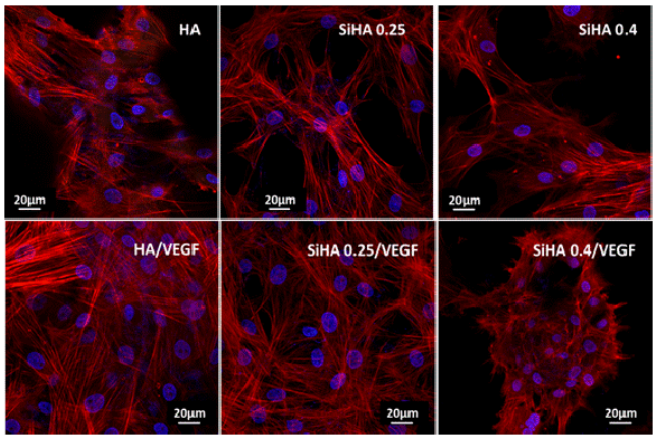

Figure 8. Morphology of EPC-derived cells on disks of crystalline HAs with different Si proportions with or without adsorbed VEGF (2.5 µg) observed by confocal microscopy after 5 days of culture. Actin was stained with rhodamine-phalloidin (red) and cell nuclei with DAPI (blue).

The present study demonstrates that adsorbed VEGF on nanocrystalline and crystalline HAs can exert a local regulation of the cell response in agreement with previous work by others.[4-7] On the other hand, the effects of the different Si proportions and nanocrystallinity on the proliferation of EPCs when cultured on disks with adsorbed VEGF (2.5 µg) can be observed in **Figure 9B**. The comparisons between each nanocrystalline and crystalline HA with different Si proportions and with adsorbed VEGF (2.5 µg) show that the cell number was higher on crystalline materials. This fact could be related to the different crystallite size and textural parameters of nanocrystalline HAs in comparison to crystalline HAs (Table 1). The topography of nanocrystalline materials could produce insufficient and weak contacts between the EPCs and the surface of nanocrystalline HAs which can trigger a kind of apoptosis defined as anoikis, that is induced by the loss of cell/matrix interactions.[59] Concerning the Si proportion, the best results were obtained with SiHA/VEGF disks containing x = 0.25 of Si, with significantly superior proliferation than in any other disk type including respective nano-SiHA. In this sense, Si seems to play a beneficial role on the EPC proliferation. However, this effect is limited to certain levels of substitution in the HA structure. Nano-SiHA0.4 and SiHA0.4 samples evidence a significant decrease in cell proliferation compared with nano-SiHA0.25 and SiHA0.25. In the latest samples, the amount of Si incorporated is enough to yield changes in the textural parameters and surface charge without decompose the HA phase. However, silicon substitution for x = 0.4 did not result in pure Si-substituted apatites. Since the HA structure cannot admit such a high number of vacancies at the OH positions and crystal-chemical defects, Si probably remains at the grain boundaries as amorphous silica in nano-SiHA0.4.[47]

After the thermal treatment at 1150 ºC, SiHA0.4 is decomposed in α-TCP and HA and resulted in materials with a higher degree of microstructural defects. None of these scenarios seemed to favour the proliferation of EPCs. On the contrary, the incorporation of smaller amounts of Si, such as x = 0.25, resulted in stable Si-substituted apatites that improved the proliferation of the endothelial cells seeded on it.

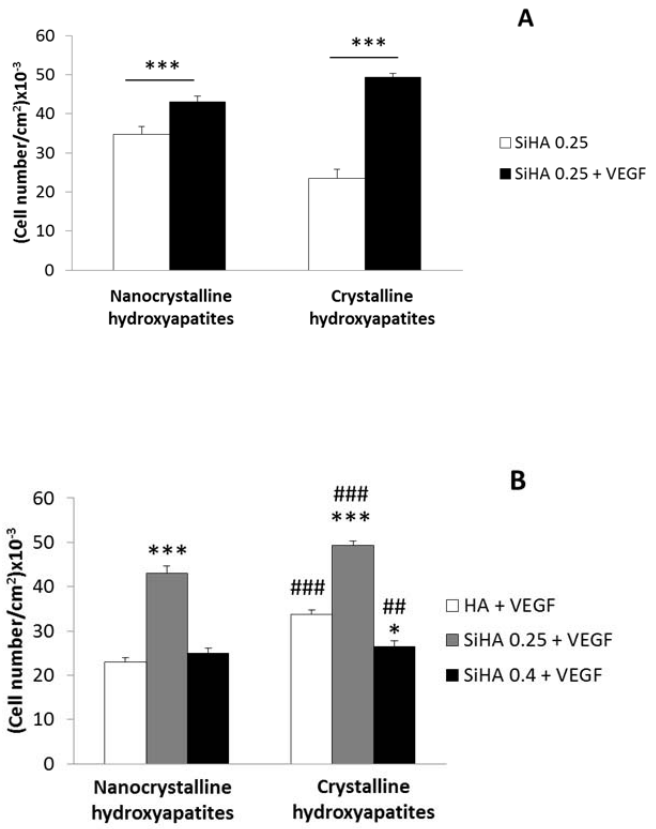

Figure 9. EPC-derived cell proliferation on disks of nanocrystalline and crystalline hydroxyapatites with or without adsorbed VEGF. **(A)** Proliferation on nanocrystalline and crystalline SiHA 0.25 silicon substituted hydroxyapatites with or without adsorbed VEGF (2.5 µg). * Comparison between each material with or without adsorbed VEGF. Statistical significance: *** $p < 0.005$. **(B)** Proliferation on nanocrystalline and crystalline hydroxyapatites with different Si proportion and with adsorbed VEGF (2.5 µg). * Comparison between each silicon substituted hydroxyapatite and hydroxyapatyte, # Comparison between each nanocrystalline and crystalline hydroxyapatite. Statistical significance: ***, ### $p < 0.005$, ## $p < 0.01$, * $p < 0.05$.

As the disks containing a proportion of 0.25 of Si more significantly promoted cell proliferation, we then explored the morphology of EPC-derived EC1 cells cultured on these disks (nano-SiHA0.25 and SiHA0.25), with or without immobilized

VEGF, by SEM after 5 days of culture. Interestingly, in another study to determine the osteogenic capability of SiHA, Hing et al[60] obtained the best results with SiHA substituted with a very similar silicon content (0.8 % wt) respect to our SiHA0.25 (which contains a 0.7 % wt of silicon), demonstrating that these silicon levels elicited an optimal effect on the activity of bone forming and bone resorbing cells. Our studies demonstrate that, in addition to the effect on osteoblast and osteoclast, this silicon content is also optimal for the regulation of endothelial cells.

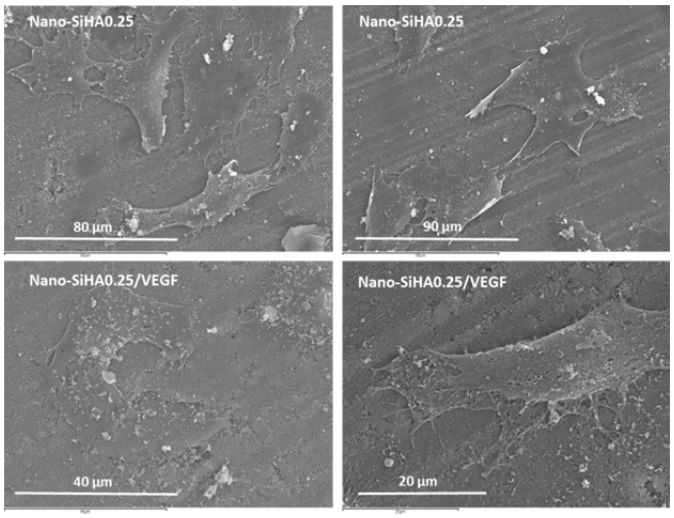

Figure 10. Morphology of EPC-derived cells on disks of nano-SiHA0.25 with or without adsorbed VEGF (2.5 µg) as observed by SEM after 5 days of culture.

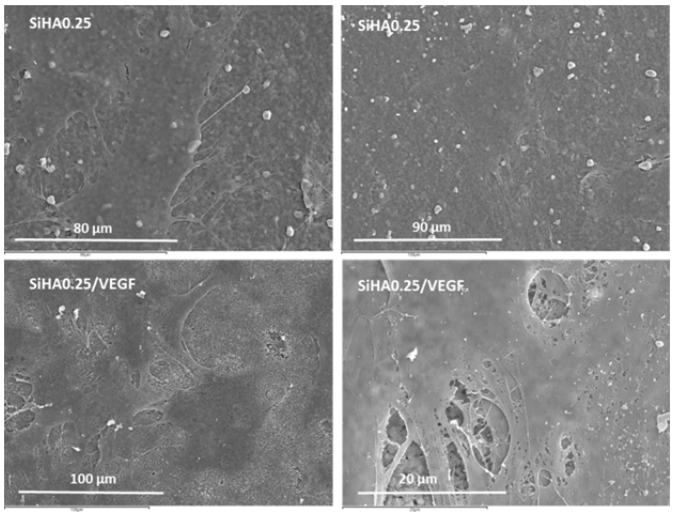

Figure 11. Morphology of EPC-derived cells on disks of SiHA0.25 with or without adsorbed VEGF (2.5 µg) observed by SEM after 5 days of culture.

SEM images demonstrated the presence of cells attached on these four materials, with the typical morphological features of this cell type (**Figures 10** and **11**). However, a higher number of cells attached on SiHA0.25 disks, rather than on nano-SiHA0.25 disks were observed with and without VEGF, showing a better EPC-derived EC1 cell adhesion to the surface of crystalline SiHA. These results could be related to the different topography of nanocrystalline SiHA0.25 inducing anchorage loss of cells on its surface. On the other hand, structures suggesting the presence of fenestrae, typical of endothelial cells,[61] were observed in some of the EC1 cells growing on SiHA0.25/VEGF (**Figure 11** lower panel right). The fenestrae act as a selective barrier to control the exchange between the blood and the cells of the tissues, mainly present in the liver sinusoidal endothelial cells.[61] These structures are transcytoplasmic canals which can be induced in vascular endothelial cells upon stimulation with VEGF,[62,63] as observed in this work.

Conclusions

Immobilized VEGF on disks of crystalline and nanocrystalline HAs with different Si proportions maintained its function and exerted a local regulation of the cell response improving EPC-derived endothelial cell adhesion and proliferation. The best results were obtained with SiHA0.25/VEGF and nano-SiHA0.25/VEGF disks, suggesting the potential utility of these Si-substituted HAs with immobilized VEGF for bone repair and tissue engineering by promoting angiogenesis.

Acknowledgements

This study was supported by research grants from the Ministerio de Economía y Competitividad (projects MAT2013-43299-R and MAT2015-64831-R) and Agening Network of Excellence (CSO2010-11384-E). MCM is greatly indebted to MEC for predoctoral fellowship. MCS acknowledges the Instituto de Salud Carlos III for a Miguel Servet I contract (MS13/00060). The authors wish to thank also to the staff of the ICTS Centro Nacional de Microscopía Electrónica (Spain) for the assistance in the scanning electron microscopy and to the staff of the Centro de Citometría y Microscopía de Fluorescencia of the Universidad Complutense de Madrid (Spain) for the assistance in the confocal laser scanning microscopy and flow cytometry studies.

References

1 D. Barati, S. R. P. Shariati, S. Moeinzadeh, J. M. Melero-Martin, A. Khademhosseini and E. Jabbar, *J. Control. Release,* 2016, **223,** 126.

2 F. M. Chen, M. Zhang and Z. F. Wu, *Biomaterials,* 2010, **31,** 6279.
3 R. R. Chen and D. J. Mooney, *Pharm. Res.,* 2003, **20,** 1103.
4 A. G. Guex, D. Hegemann, M. N. Giraud, H. T. Tevaearai, A. M. Popa, R. M. Rossi and G. Fortunato, *Colloid. Surface. B,* 2014, **123,** 724.
5 M. J. Feito, R. M. Lozano, M. Alcaide, C. Ramírez-Santillán, D. Arcos, M. Vallet-Regí and M. T. Portolés, *J. Mater. Sci. Mater. Med.,* 2011, **22,** 405.
6 M. C. Matesanz, M. J. Feito, C. Ramírez-Santillán, R. M. Lozano, S. Sánchez-Salcedo, D. Arcos, M. Vallet-Regí and M. T. Portolés, *Macromol. Biosci.,* 2012, **12,** 446.
7 D. Lozano, M. J. Feito, S. Portal-Nuñez, R. M. Lozano, M. C. Matesanz, M. C. Serrano, M. Vallet-Regí, M. T. Portolés and P. Esbrit, *Acta Biomater.,* 2012, **8,** 2770.
8 S. B. Fox, G. Gasparini and A. L. Harris, *Lancet Oncol.,* 2001, **2,** 278.
9 N. Ferrara, H. Gerber and J. LeCouter, *Nat. Med.,* 2003, **9,** 669.
10 C. J. Robinson and S. E. Stringer, *J. Cell Sci.,* 2001, **114,** 853.
11 N. Ferrara and T. Davis-Smyth, *Endocr. Rev.,* 1997, **18,** 4.
12 K. Alitalo and P. Carmeliet, *Cancer Cell.,* 2002, **1,** 219.
13 G. Niu and X. Chen, *Curr. Drug Targets,* 2010, **11,** 1000.
14 A. G. Guex, D. Hegemann, M. N. Giraud, H. T. Tevaerai, A. M. Popa, R. M. Rossi and G. Fortunato, *Colloid. Surface. B,* 2014, **123,** 724.
15 K. S. Maters, *Macromol. Biosci.,* 2011, **11,** 1149.
16 N. Rozen, T. Bick, A. Bajayo, B. Shamian, M. Schrift-Tzadok, Y. Gabet, A. Yayon, I. Bab, M. Soudry and D. Lewinson, *Bone,* 2009, **45,** 918.
17 Y. Q. Yang, Y. Y. Tan, R. Wong, A. Wenden, L. K. Zhang and A. B. M. Rabie, *Int. J. Oral Sci.,* 2012, **4,** 64.
18 J. P. Levesque, F. M. Helwani and I. G. Winkler, *Leukemia,* 2010, **24,** 1979.
19 J. Street, M. Bao, S. Bunting, F. V. Peale, N. Ferrara, H. Steinmetz, J. Hoeffel, J. L. Cleland, A. Daugherty and N. van Bruggen, *Proc. Natl. Acad. Sci.,* 2002, **99,** 9656.
20 C. Kalka, H. Masuda, T. Takahashi, W. M. Kalka-Moll, M. Silver, M. Kerany, T. Li, J. M. Isner and T. Asahara, *Proc. Natl. Acad. Sci. USA,* 2000, **97,** 3422.
21 A. Papathanasopoulos and P. V. Giannoundis, *Injury,* 2008, **39S2,** S21.
22 M. C. Serrano, R. Pagani, M. Vallet-Regí, J. Peña, J. V. Comas and M. T. Portolés, *Acta Biomater.,* 2009, **5,** 2045.
23 M. S. Chong, W. K. Ng and J. K. Chan, *Stem Cells Transl. Med.,* 2016, **5,** 530.
24 M. M. Tenreiro, R. Ferreira, L. Bernardino and M. A. Brito, *Neurobiol. Dis.,* 2016, **91,** 262.
25 H. Zigdon-Giladi, U. Rudich, G. Michaeli Geller and A. Evron, *World J. Stem Cells,* 2015, **7,** 630.
26 H. Zhou and J. Lee, *Acta Biomater.,* 2011, **7,** 2769.
27 R. Bosco, J. Van Den Beucken, S. Leeuwenburgh and J. Jansen, *Coatings,* 2012, **2,** 95.
28 J. H. Shepherd, D. V. Shepherd and S. M. Best, *J. Mater. Sci. Mater. Med.,* 2012, **23,** 2335.
29 A. M. Pietak, J. W. Reid and M. J. Stott, *Biomaterials,* 2007, **28,** 4023.
30 M. Bohner, *Biomaterials,* 2009, **30,** 6403.
31 F. Balas, J. Pérez-Pariente and M. Vallet-Regí, *J. Biomed. Mater. Res. A*, 2003, **66,** 364.
32 A. E. Porter, S. M. Best, and W. Bonfield, *J. Biomed. Mater. Res. A,* 2004, **68,** 133.
33 M. Vallet-Regí, and D. Arcos, *J. Mater. Chem.,* 2005, **15,** 1509.
34 S. V. Dorozhkin, *Materials,* 2009, **2,** 1975.
35 N. Patel, S. M. Best, W. Bonfield, I. R. Gibson, K. A. Hing, E. Damien, E. and P. A. Revell, *J. Mater. Sci. Mater. Med.,* 2002, **13,** 1199.
36 M. I. Kay, R. A. Young and A. S. Posner, *Nature,* 1964, **204,** 1050.
37 J. Rodríguez-Carvajal, *Physica B,* 1993, **192,** 55.
38 P. Thompson, D. E. Cox and J., B. Hastings, *J. Appl. Cryst.,* 1987, **20,** 79.
39 S. Brunauer, P. H. Emmett and E. Teller, *J. Am. Chem. Soc.,* 1938, **60,** 309.
40 E. P. Barret, L. J. Joyner and P. P. Halenda, *J. Am. Chem. Soc.,* 1951, **73,** 373.
41 M. C. Serrano, R. Pagani, G. A. Ameer, M. Vallet-Regí and M. T. Portolés, *J. Biomed. Mater. Res. A,* 2008, **87,** 964.
42 S. Samavedi, A. R. Whittington and A. S. Goldstein, *Acta Biomater.,* 2013, **9,** 8037.
43 A. E. Porter, N. Patel, J. N. Skepper, S. M. Best, and W. Bonfield, *Biomaterials,* 2003, **24,** 4609.
44 S. V. Dorozhkin, *Materials,* 2009, **2,** 1975.
45 E. S. Thian, Z. Ahmad, J. Huang, M. J. Edirisinghe, S. N. Jayasinghe, D. C. Ireland, R. A. Brooks, N. Rushton, W. Bonfield, and S. M. Best, *Acta Biomater.,* 2010, **6,** 750.
46 M. C. Matesanz, M. J. Feito, M. Oñaderra, C. Ramírez-Santillán, C. da Casa, D. Arcos, M. Vallet-Regí, J. M. Rojo and M. T .Portolés, *J. Colloid Interf. Sci.,* 2014, **416,** 59.
47 D. Arcos, J. Rodríguez-Carvajal and M. Vallet-Regí, *Chem. Mater.,* 2004, **16,** 2300.
48 S. V. Dorozhkin, *Biomaterials,* 2010, **31,** 1465.
49 S. Langstaff, M. Sayer, T. J. N. Smith, S. M. Pugh, S. A. M. Hesp and W. T. Thompson, *Biomaterials,* 1999, **7,** 1727.
50 I. R. Gibson, S. M. Best and W. Bonfield, *J. Biomed. Mater. Res.,* 1999, **44,** 422.
51 J. Amirian, N. T. B. Linh, Y. K. Min and B. T. Lee, *Int. J. Biol. Macromol.,* 2015, **76,** 10.
52 M. B. Gorbet and M. V. Sefton, *Biomaterials,* 2004, **25,** 5681.
53 A. Rosengren, E. Pavlovic, S. Oscarsson, A. Krajewski, A. Ravaglioli and A. Piancastelli, *Biomaterials,* 2002, **23,** 1237.
54 Y. Wang, G. Subbiahdoss, J. de Vries, M. Libera, H. C. van der Mei and H. J. Busscher, *Biofouling,* 2012, **28,** 1011.
55 C. Tedjo, K. G. Neoh, E. T. Kang, N. Fang and V. Chan, *J. Biomed. Mater. Res. A,* 2007, **82,** 479.
56 H. Chen, L. Yuan, W. Song, Z. Wu and D. Li, *Prog. Polym. Sci.,* 2008, **33,** 1059.
57 M. C. Matesanz, J. Linares, M. Oñaderra, M. J. Feito, F. J. Martínez-Vázquez, D. Arcos, S. Sánchez-Salcedo, M. T. Portolés and M. Vallet-Regí, *Colloid. Surface. B,* 2015, **133,** 304.
58 K. Walenta, E. B. Friedrich, F. Sehnert, N. Werner and G. Nickenig, *Biochem. Biophys. Res. Commun.,* 2005, **333,** 476.
59 S. M. Frisch and R. A. Screaton RA, *Curr. Opin. Cell Biol.,* 2001, **13,** 555.
60 K.A. Hing, P.A. Revell, N. Smith, T. Buckland, *Biomaterials*, 2006, **27**, 5014.
61 B. Vollmar and M. D. Menger, *Physiol. Rev.,* 2009, **89,** 1269.
62 S. Esser, K. Wolburg, H. Wolburg, G. Breier, T. Kurzchalia and W. Risau, *J. Cell. Biol.,* 1998, **140,** 947.
63 J. Funyu, S. Mochida, M. Inao, A. Matsui and K. Fujiwara, *Biochem. Biophys. Res. Commun.,* 2001, **280,** 481.